Remote Sensing of Environment 237 (2020) 111543

Contents lists available at ScienceDirect

Remote Sensing of Environment

journal homepage: www.elsevier.com/locate/rse

Structural characterisation of mangrove forests achieved through combining multiple sources of remote sensing data

Richard Lucas[a,b,*], Ruben Van De Kerchove[c], Viviana Otero[d], David Lagomasino[f,g], Lola Fatoyinbo[g], Hamdan Omar[e], Behara Satyanarayana[h,i], Farid Dahdouh-Guebas[d,i]

[a] Department of Geography and Earth Sciences, Aberystwyth University, Aberystwyth, Ceredigion SY23 3DB, United Kingdom
[b] Centre for Ecosystem Science (CES), School of Biological, Earth and Environmental Sciences (BEES), University of New South Wales, High Street, Kensington, NSW 2052, Australia
[c] Vlaamse Instelling Voor Technologisch Onderzoek (VITO) Research Organisation, Mol, Belgium
[d] Systems Ecology and Resource Management Research Unit, Department of Organism Biology, Université Libre de Bruxelles (ULB), Av. F.D. Roosevelt 50, CPi 264/1, B-1050 Brussels, Belgium
[e] Division of Forestry & Environment, Forest Research Institute Malaysia (FRIM), 52109, Kepong, Selangor, Malaysia
[f] Department of Coastal Studies, East Carolina University, 850 NC-345, Wanchese, NC 27981, USA
[g] Biospheric Sciences Laboratory, Code 618, NASA Goddard Space Flight Center, 8800 Greenbelt Road, Greenbelt, MD 20771, USA
[h] Mangrove Research Unit, Institute of Oceanography and Environment, Universiti Malaysia Terengganu (UMT), Kuala Terengganu, Malaysia
[i] Laboratory of Plant Biology and Nature Management, Ecology & Biodiversity, Vrije Universiteit Brussel (VUB), VUB-APNA-WE, Pleinlaan 2, B-1050 Brussels, Belgium

ARTICLE INFO

Edited by: Emilio Chuvieco

Keywords:
Remote sensing
Mangroves
Time-series
Forest structure
Management

ABSTRACT

Temporal information on mangrove extent, age, structure and biomass provides an important contribution towards understanding the role of these ecosystems in terms of the services they provide (e.g., in relation to storage of carbon, conservation biodiversity), particularly given the diversity of influences of human activity and natural events and processes. Focusing on the Matang Mangrove Forest Reserve (MMFR) in Perak Province, Peninsular Malaysia, this study aimed to retrieve comprehensive information on the biophysical properties of mangroves from spaceborne optical and Synthetic Aperture Radar (SAR) to support better understanding of their dynamics in a managed setting. For the period 1988 to 2016 (29 years), forest age was estimated on at least an annual basis by combining time-series of Landsat-derived Normalised Difference Moisture Index (NDMI) and Japanese L-band Synthetic Aperture Radar (SAR) data. The NDMI was further used to retrieve canopy cover (%). Interferometric Shuttle Radar Topographic Mission (SRTM) X/C-band (2000), TanDEM-X-band (2010–2016) and stereo WorldView-2 stereo (2016) data were evaluated for their role in estimating canopy height (CH), from which above ground biomass (AGB, Mg ha^{-1}) was derived using pre-established allometry. Whilst both L-band HH and HV data increased with AGB after about 8–10 years of growth, retrieval was compromised by mixed scattering from varying amounts of dead woody debris following clearing and wood material within regenerating forests, thinning of trees at ~15 and 20 years, and saturation of L-band SAR data after approximately 20 years of growth. Reference was made to stereo Phantom-3 DJI stereo imagery to support estimation of canopy cover (CC) and validation of satellite-derived CH. AGB estimates were compared with ground-based measurements. Using relationships with forest age, both CH and AGB were estimated for each date of Landsat or L-band SAR observation and the temporal trends in L-band SAR were shown to effectively track the sequences of clearing and regeneration. From these, four stages of the harvesting cycle were defined. The study provided new information on the biophysical properties and growth dynamics of mangrove forests in the MMFR, inputs for future monitoring activities, and methods for facilitating better characterisation and mapping of mangrove areas worldwide.

1. Introduction

Understanding mangrove dynamics in response to both natural and human-induced disturbance has often been addressed using Earth Observation (EO) data and by largely considering changes in extent over time (Asbridge et al., 2015; Richards and Friess, 2016; Thomas et al., 2017; Lagomasino et al., 2019). The capacity to undertake such analyses has increased with the release of archives of optical (e.g.

* Corresponding author at: Department of Geography and Earth Sciences, Aberystwyth University, Aberystwyth, Ceredigion SY23 3DB, United Kingdom.
E-mail address: richard.lucas@aber.ac.uk (R. Lucas).

https://doi.org/10.1016/j.rse.2019.111543
Received 12 June 2019; Received in revised form 5 November 2019; Accepted 14 November 2019
Available online 06 December 2019

Landsat) and, more recently, Synthetic Aperture Radar (SAR) satellite sensor data that have a high frequency of observations (Lymburner et al., 2019). This high spatio-temporal frequency provides the capacity to track inter and intra-annual variability with finer fidelity. The capacity to interrogate the three-dimensional structure of mangroves at multiple scales has also improved with the provision of airborne and spaceborne stereo viewing capability, Light Detection and Ranging (LIDAR) and interferometric SAR (Simard et al., 2018; Lee and Fatoyinbo, 2015; Lagomasino et al., 2016).

Focusing on the Matang Mangrove Forest Reserve (MMFR) in Perak Province, Peninsular Malaysia, this research aimed to better quantify and understand mangrove dynamics in response to forest management by integrating time-series of Japanese L-band SAR and Landsat sensor, interferometric X/C-band SAR and WorldView-2 stereo data, with validation provided primarily by stereo drone (RGB) imagery and field measurements. The MMFR provided a unique setting as the area is comprised of mangroves of varying age, including relatively undisturbed (protective forest), naturally regenerating forests and those recovering from timber extraction (productive forest for charcoal and pole production; Ariffin and Mustafa, 2013). Harvesting has taken place since 1902 on a nominal 30-year rotation (as stated in the MMFR management plans; Noakes, 1952). The specific objectives of the paper were to:

a) Estimate the age of mangrove forests (primarily within the productive zone) across the MMFR through integration of time-series of Landsat sensor and Japanese L-band HH and/or HV SAR data.
b) Investigate the reliability of canopy height (CH) retrieval from both interferometric SAR and high-resolution spaceborne stereo optical imagery and determine whether relationships with CH could be used to estimate above-ground biomass (AGB, Mg ha^{-1}) across the MMFR.
c) Determine changes in CH (and by inference AGB) as a function of forest age, to establish whether CH could be predicted from age alone.
d) Track changes in the L-band backscattering coefficient (Sigma0; σ°, dB) as a function of CH and age and establish potential for retrieving forest AGB.
e) Investigate whether a reported decline in L-band backscattering (Lucas et al., 2007; Asbridge et al., 2016; particularly at HH polarisation) over time was in proportion to CH and aligned with the development and maturing of the prop root systems of *Rhizophora* species

The following sections provide details of the MMFR, an overview of available remote sensing data, approaches to the retrieval of forest age, structure and AGB from these, and the resulting map products with associated validation. Stages in the nominal 30-year harvesting cycle are then defined in relation to the temporal trajectories of satellite sensor data and derived products. The contribution of EO from a diversity of sensors for characterising and mapping mangroves is then discussed together with implications for developing mangrove monitoring systems to support forest management and sustainable utilization.

2. Study area

The MMFR is located on the west coast of Peninsular Malaysia (02°30′N, 112°30′E; Fig. 1). The climate regime of the Peninsula is tropical with monsoons occurring from April to October (blowing towards the southwest) and October to February (the northeast). The area receives an annual rainfall ranging from 2000 to 2800 mm and average diurnal air temperatures from 22 to 33 °C. The coastal margin is largely of low elevation but is interspersed with steep hills comprised primarily of limestone. Protection from ocean waves and tidal influences (spring tide amplitude of 3.3 m) has allowed extensive mangrove forests to colonise and thrive along the coastline. Within the MMFR, mangroves occupy an area of 40,466 ha, and 11 true mangrove families (28 species) and 10 associate mangrove families (13 species) occur. The dominant species are *Rhizophora mucronata* Lamk. and *R. apiculata* Bl., *Sonneratia alba* J. Smith, *Bruguiera gymnorrhiza* (L.) Lamk. and *B. cylindrica* (L.) Blume and *Avicennia marina* (Forssk.) Vierh.. These mangroves enclose or adjoin transitional dryland forest, with these dominated by *Acrostichum* ferns. *Nypa fruticans* (Thunb.) Wurmb., a palm, is frequent along the river margins.

The MMFR is composed of a patchwork of coupes, each of a different age but logged on a nominal 30-year rotation. The latter involves complete clearing of each forest coupe, after which subsequent forest growth within coupes takes place through a combination of replanting and/or natural regeneration depending on site conditions. After ~15 and 20 years of regrowth, the forests are thinned (Ariffin and Mustafa, 2013) and harvested again once the forests have reached maximum productivity (i.e., at ~30 years). The management has favoured the establishment of *Rhizophora apiculata* and *R. mucronata*, which has resulted in coupes with relatively even-aged monocultures of these two species. These two mangrove species dominate the productive forests of the MMFR. The protective forests have remained relatively undisturbed from human activities for over 100 years.

3. Methods

3.1. Available data

For the study, all available Landsat Thematic Mapper (TM) and Enhanced TM+ data acquired over the period 29th July 1988 to 29th September 2016 were obtained as surface reflectance products from the United States Geological Survey (USGS). All available Japanese Earth Resources Satellite (JERS-1) SAR (HH polarisation), Advanced Land Observing Satellite (ALOS) Phased Arrayed L-band SAR (PALSAR); both Fine beam Single (FBS; HH) and Fine Beam Dual (FBD; HH and HV), and ALOS-2 PALSAR-2 FBS and FBD data were obtained through the Japanese Space Exploration Agency (JAXA) Kyoto and Carbon (K&C) Initiative for three epochs (1993–1997, 2006–2011 and 2014–2016 respectively). The incidence angles varied between the JERS-1 SAR (36–42°), ALOS PALSAR (36.6–40.9°) and the ALOS-2 PALSAR-2 (33.7–38.5° and 38.3–42.5°; for beams 6 and 7 with off-nadir angles of 32.5° and 36.2° respectively). The number and date distribution of scenes from both the Landsat sensors and Japanese L-band SAR is given in Fig. 2. NASA Shuttle Radar Topographic Mission (SRTM) data were acquired between the 11th and 22nd February 2000, TanDEM-X between 23rd January 2011 and 2nd October 2015 (but corresponding to 2015 based on comparisons of clearing patterns within the optical and SAR data), and commercial WorldView-2 data on January 23th 2016.

To support the retrieval of biophysical variables from the spaceborne data, reference was made to forest inventory data collected in June, July and December 2016 and April 2017 and included measurements of tree and size (diameter, height; Otero et al., 2018). In July 2016, digital images were obtained for 1-hectare (ha) areas containing the field plots using a DJI Phantom 3 Professional quadcopter Unmanned Airborne Vehicle (UAV) and the in-built true colour (RGB) camera in July 2016 (Otero et al., 2018).

Existing estimates of stand level AGB were obtained for 2010 and 2011 (Hamdan et al., 2013) from 114, 20 m × 50 m sample plots located within the MMFR. These plots were measured within undisturbed as well as managed (productive) forests under varying degrees of maturity. Within the plots, all trees with diameters ≥5 cm at breast height (D_{130} or 30 cm above the highest prop root for *Rhizophora* spp.) were measured. All trees were identified to species noting that, within the managed forests, over 90% of the trees are dominated by *Rhizophora* species (primarily *R. apiculata*) with *Avicennia*, *Sonneratia* and *Bruguiera* species sometimes occurring. The sample plots were located in areas that were easily accessible and safe to enter. The plot-level AGB was

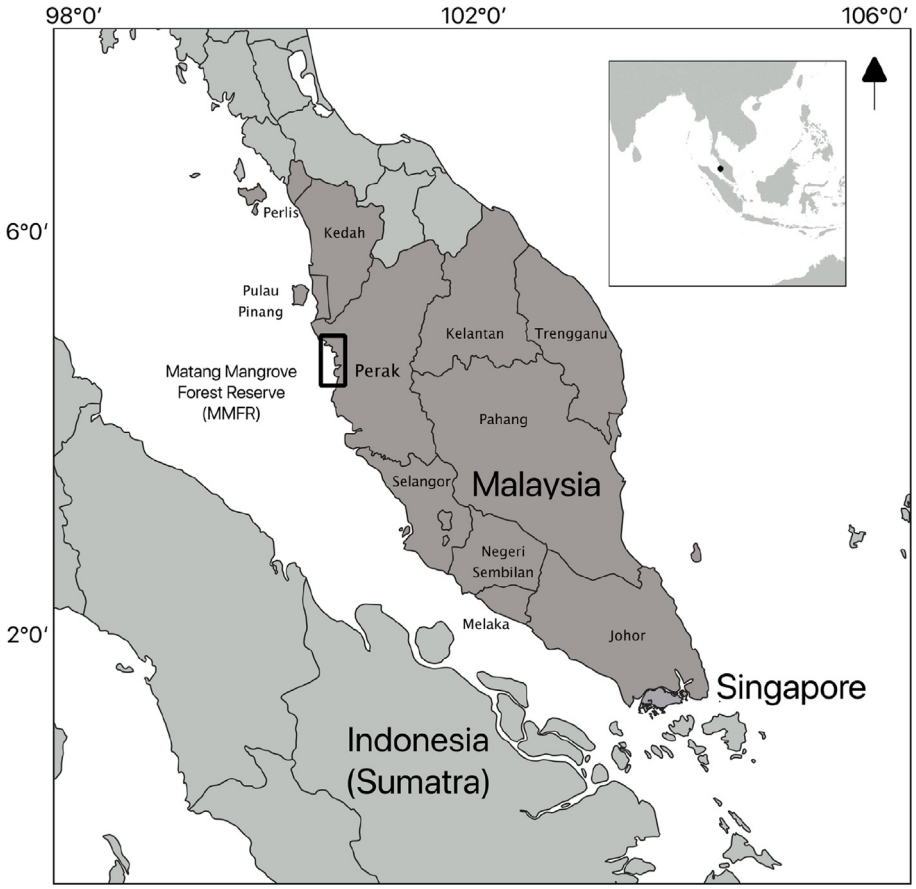

Fig. 1. The location of the Matang Mangrove Forest Reserve (MMFR) in Peninsular Malaysia.

estimated using the equations of Ong et al. (2004), Komiyama et al. (2008) and Clough and Scott (1989) for *R. apiculata*, *Avicennia. alba* Blume (using a wood density of 0.506 g cm^{-3}) and *B. parviflora* respectively.

3.2. Data analysis

3.2.1. Landsat calibration and derivation of indices

For most years and from 1987 onwards, single Landsat images that were entirely or largely free of cloud were obtained. However, where cloud was persistent in some years, available data were combined to generate annual reflectance image composites for the MMFR. From these data, the Normalised Difference Vegetation Index (NDVI) and Normalised Difference Moisture Index (NDMI) were derived (Schmidt et al., 2013). These two indices were selected as they increased from low values associated with recently cleared forests to a maximum associated with canopy closure, suggesting a potential link with canopy cover.

Individual JERS-1 SAR L-band HH and both ALOS PALSAR and ALOS-2 PALSAR-2 L-band HH and HV scenes were speckle filtered. The L-band SAR digital numbers (DN) were calibrated to the σ° using equations listed in Table 1 (Shimada et al., 2009), with the bands referred to as $L_{HH}\sigma^{\circ}$ and $L_{HV}\sigma^{\circ}$ from hereon in.

To establish the framework for collating and combining both optical and radar data and derived products on the MMFR, the KEA format (Gillingham and Bunting, 2014) was used, which exploits raster attribute tables to store information. To create a KEA format file, a segmentation algorithm was applied to generate segments that typically contained < 5 pixels of 12 m × 12 m resolution (for testing) and subsequently at the pixel level (for implementation). Each segment was then populated with both the Landsat NDVI, and NDMI, Japanese L-band SAR data and other attributes (e.g., CH from interferometric SAR) in date order.

3.2.2. Estimation of mangrove forest age

To estimate the age of mangroves within the MMFR, forest and non-forest areas were mapped on an annual or sub-annual basis by applying thresholds to the time-series of Landsat NDMI (1988–2016) and $L_{HH}\sigma^{\circ}$ data. The NDMI and $L_{HH}\sigma^{\circ}$ showed greater contrast between pre-cleared and cleared areas compared to the NDVI and $L_{HV}\sigma^{\circ}$ respectively (Otero et al., 2019). For each year from 1988 to 2016, the cloud-free single scenes or annual composites of Landsat sensor data were selected, with the latter stamped with the date of the scene contributing the most cloud-free pixels. The Japanese L-band SAR data were used to provide better timing of clearing within each of the three epochs (i.e., 1993–1997, 2006–2011 and 2014–2016) as sub-annual cloud-free data were available for each year. Some images were acquired only a few weeks apart were compared and often no changes were detected. An evaluation of these $L_{HH}\sigma^{\circ}$ data revealed that clearings were particularly distinct but also that each logging coupe was cleared over several years rather than at the same time, with this attributed to the allocation of different sections of the coupes to different logging companies or groups. For example, several logging coupes were progressively cleared over a period of ~24 months over the period from August 2007 to January 2011 (Fig. 3). Of note is that several of the areas with a higher $L_{HH}\sigma^{\circ}$ in 2007 had experienced a decline in σ° by 2011.

To map logged areas, thresholds of the NDMI and $L_{HH}\sigma^{\circ}$ were used to identify the conversion of forest to non-forest. This conversion was only recorded when the Landsat-derived NDMI or $L_{HH}\sigma^{\circ}$ was above or below the threshold defined for mature forest in the first image of each two consecutive date comparisons (typically between −7.2 to −9.0 dB and 0.32 to 0.39 respectively) but then was less or greater than the

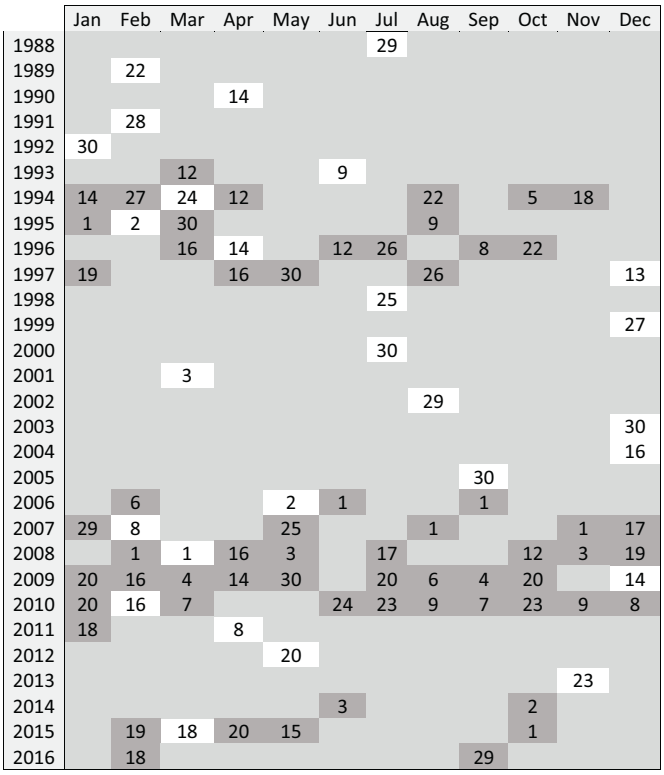

Fig. 2. The 98 acquisition dates of JERS-1 SAR (1993–1997), ALOS PALSAR (2006–2011) and ALOS-2 PALSAR-2 (2015–2016) (grey) and Landsat sensor data (white) acquired for the MMFR. The numbers represent the dates of image acquisition. Landsat sensor and ALOS PALSAR data were acquired on the 1st March 2018. ALOS PALSAR data were also acquired on the 29th April 2009, 30th August and 30th November 2007, 14th and 18th March 2009, 5th 14th and 22nd December 2019, 25th December 2010 and 23th Jan 2011.

Table 1
Equations used to convert L-band SAR digital numbers (DN) to backscattering coefficients and for generating the NDVI and NDMI.

Sensor	Polarisation	Equation
Landsat	NDVI	$\frac{(R_{NIR} - R_{Red})}{(R_{NIR} + R_{RED})}$
Landsat	NDMI	$\frac{(R_{NIR} - R_{SWIR})}{(R_{NIR} + R_{SWIR})}$
JERS-1 SAR	HH	$10*\log(DN^2) - 85.34$
ALOS PALSAR	HH and HV	$10*\log(DN^2) - 83.0$
ALOS-2 PALSAR-2	HH and HV	$10*\log(DN^2) - 83.0$

threshold in the second image. All thresholds were determined through visual interpretation, noting that these were within a narrow range because of the strong contrast between the pre- and post-cleared forests and introduction of large errors when values either side of these thresholds was used. The age of forests in days was then estimated in terms of number of days since the acquisition of the first Landsat image in the time series (29th July 1988), with this allowing sub-annual (e.g., monthly) and annual ages to be assigned subsequently. Japanese L-band SAR data with partial coverage were included and age estimates for each date were updated only for those areas with valid data.

3.2.3. Canopy height Models

To retrieve information on the stand height of mangroves, canopy height models (CHMs) were derived for both 2000 and 2015 using interferometric SAR. An additional CHM for 2016 was also retrieved from WorldView-2 stereo pair (Fig. 4). The 2015 CHMs were validated against those generated from stereo drone (RGB) imagery acquired in July 2016 using the Structure from Motion (SfM) algorithm (Otero et al., 2018).

3.2.3.1. Shuttle Radar Topography Mission. For 2000, the CH for mangroves within the MMFR was determined from Shuttle Radar Topography Mission (SRTM) data (ground resolution of 30 × 30 m). The maximum mangrove CH ($SRTM_{CHM}$) was estimated using methods outlined in Simard et al. (2018). First elevation bias was removed from the SRTM data by using 57,369 IceSat GLAS spaceborne lidar waveforms. By applying the bias-correction, the top-of-canopy height $SRTM_{CHM}$ was estimated using

$$SRTM_{CHM} = 1.697 \times H_{SRTM} \quad (1)$$

where 1.697 is the correction and H_{SRTM} is the elevation from SRTM.

3.2.3.2. TanDEM-X digital elevation model. The TanDEM-X DEM product (2011–2015) developed by the German Space Agency (DLR) was also used to estimate CH (referred hereon in as TDX_{CHM}). The TanDEM-X DEM product (with a ground resolution of 12.5 m × 12.5 m) was processed through bistatic focusing, scene interferograms, and phase unwrapping to guarantee an independent measure between neighbouring pixels (Wessel, 2016). The DEM was calibrated using data from the Ice, Cloud and land Elevation Satellite (ICESat) Geoscience Laser Altimeter System (GLAS) as ground control for regions of open, non-vegetated and flat terrain. Block adjustments were made by automatically selecting tie points in overlapping areas of neighbouring scenes, determining offsets and tilts, and quantifying differences between the ground control points and the DEM before and after calibration. The DEMs were then mosaicked using all available scenes, with this followed by a final quality assurance by an operator. More details on the generation of the TanDEM-X DEM products can be found in Wessel (2016). To correct for elevation bias in the TDX_{CHM}, areas of bare ground were identified within the mangrove forest and a mean weighted ground elevation was subtracted from the TanDEM-X DEM, following similar methods used for very-high resolution satellite stereo-photogrammetry (Lagomasino et al., 2015).

3.2.3.3. Satellite stereophotogrammetry. One pair of Very High Resolution (2 m) stereo images from WorldView-2 (DigitalGlobe, Longmont, CO) was acquired over the MMFR on January 23, 2016. The panchromatic image pair was obtained through the NextView license agreement between Digital Globe and the National Geospatial Intelligence Agency (NGA) (Neigh et al., 2013). The image pair was acquired in "stereo-mode", whereby two images are collected using an optimized satellite viewing and sun angle geometry along the same track to reduce confounding issues related to temporal decorrelation and sensor angles. Stereophotogrammetric software and NASA Ames Stereopipeline (ASP) 2.4 software, developed by the Ames Research Center in Mountain View (California) automatically matches corresponding regions using parallax tie points. The user guide and program software are available at http://ti.arc.nasa.gov/tech/asr/intelligent-robotics/ngt/stereo/. An affine adaptive window (subpixel mode = 2) was used to estimate the most accurate surface elevation relative to the WGS84 ellipsoid. The native resolution of the DSM was approximately 0.80 m × 0.80 m, which was a function of the sensor viewing geometry of the original panchromatic images. To remove some noise, the data were resampled to a 1 m × 1 m resolution.

For mangroves, the CHM was generated from the WorldView-2 imagery (WV_{CHM}) using a method similar to Lagomasino et al. (2015, 2016). In this approach, bare ground surfaces were identified within the WV spectral image and then in the co-registered WV_{CHM}. Elevation values were then extracted from each of the identified ground surfaces and, using the area of the ground surfaces, a mean-weighted ground elevation (or Digital Terrain Model; DTM) was calculated. The DTM was the subtracted from the WV Digital Surface Model (DSM) to give the WV_{CHM}.

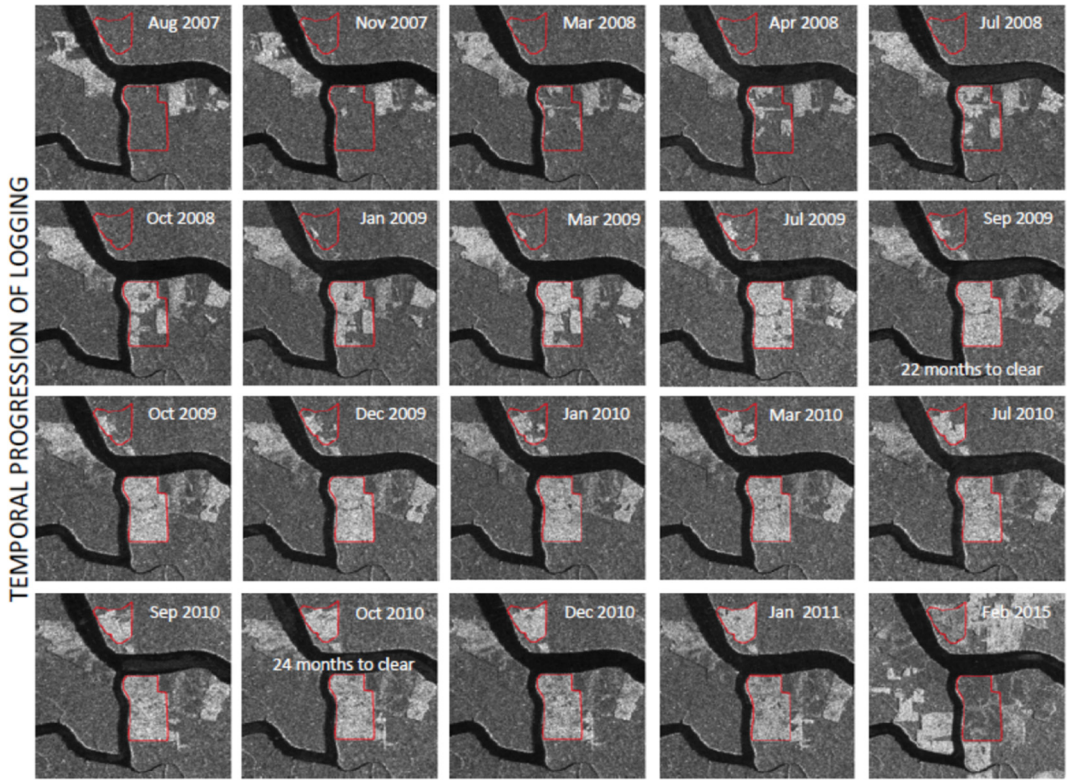

Fig. 3. Time-series of ALOS PALSAR $L_{HH}\sigma^{\circ}$ data, with high values (white) indicating the gradual clearance of logging coupes over a ~24-month period, with these contrasting with the mature forest (dark grey). Several logging coupes (as observed by the ALOS PALSAR) are highlighted in red. (For interpretation of the references to colour in this figure legend, the reader is referred to the web version of this article.)

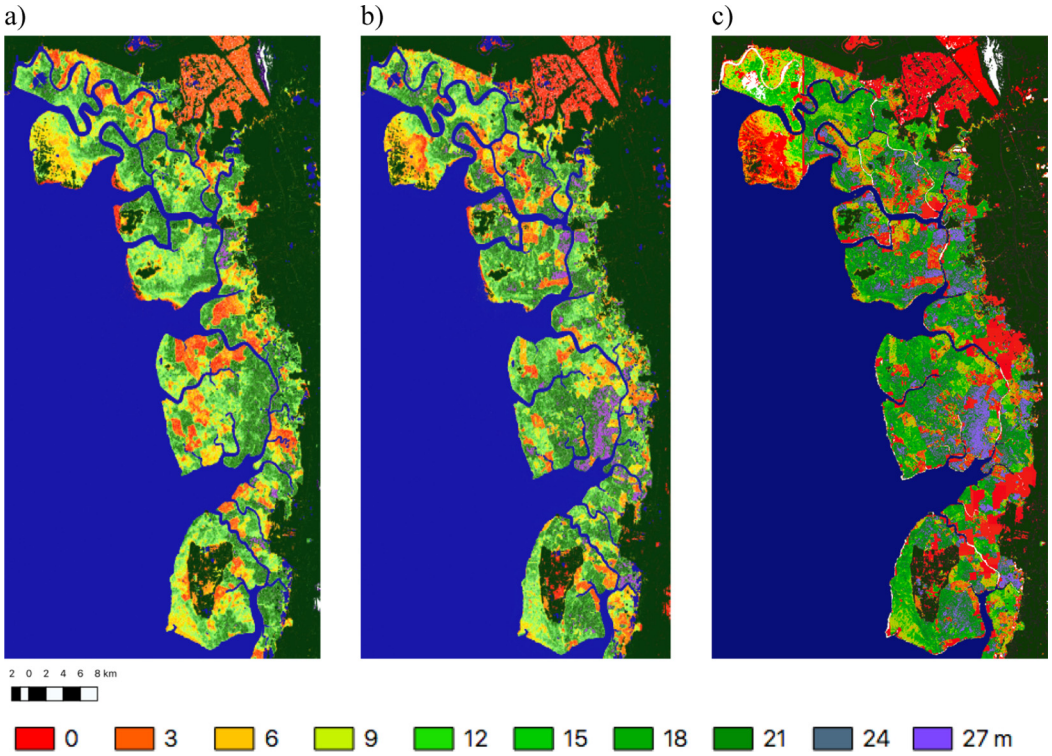

Fig. 4. Mangrove canopy height (CH) determined from a) SRTM, b) TanDEM-X DEM and c) WorldView-2 data. The latter is of lower quality, partly because of atmospheric influences.

Table 2a
Allometric equations for estimating AGB from canopy height (Simard et al., 2018).

Equation	R^2	RMSE (Mg ha^{-1})	Allometry
AGB = exp.(3.9042 + 0.0858 * H_{CHM})	0.55	148	Simard et al. (2018)

Table 2b
Allometric equations relating AGB to LH_{100} (the average height of the tallest 100 trees) (Fatoyinbo et a., 2017).

Equation	R^2	p-Value	RMSE (Mg ha^{-1})	RMSE (%)	Allometry
Linear					
32.27 ∗ (LH_{100}) − 312.8	0.85	0.000023	78	24	Chave et al. (2005)
31.45 ∗ (LH_{100}) − 254.81	0.82	0.000040	83	23	Komiyama et al. (2008)
28.02 ∗ (LH_{100}) − 217.2	0.80	0.000110	80	24	Njana et al. (2015)
Power					
AGB = 0.01 ∗ (LH_{100})3.46	0.88	0.000005	119	33	Chave et al. (2005)
AGB = 0.07 ∗ (LH_{100})2.83	0.86	0.000012	135	33	Komiyama et al. (2008)
AGB = 0.10 ∗ (LH_{100})2.7	0.85	0.000023	122	33	Njana et al. (2015)

3.2.4. Above ground biomass

For estimating AGB from CHMs, a number of global and regional equations have been used. For the $SRTM_{CHM}$, the regional (Southeast Asia) generic equation from Simard et al. (2018) is recommended (Table 2a). For the TDX_{CHM} and WV_{CHM}, linear and power relationships published for areas in East Africa were available (Fatoyinbo et al., 2017; Table 2b). These six equations were developed based on comparisons between lidar-derived height and summaries from 41 mangrove inventory plots in the Zambezi Delta in Mozambique. For each inventory plot (Stringer et al., 2015; Trettin et al., 2015), the AGB was estimated using equations from Chave et al. (2005), Komiyama et al. (2008), and Njana et al. (2015). From those field-based AGB estimates, the linear and power regression relationships with CH were formulated (Fatoyinbo et al., 2017; Table 2b). For the MMFR, all six combinations were used to estimate AGB.

3.2.5. Calibration/validation of satellite products

3.2.5.1. Forest age (months). The ages of forests were validated through reference to over 30 sites where age information based on estimates from the Perak State Forestry Department was obtained and/or for which a visual interpretation of available Landsat sensor NDMI and $L_{HH}\sigma^{\circ}$ data in the time-series was undertaken.

3.2.5.2. Canopy height (m). To validate the TDX_{CHM} and WV_{CHM}, reference was made to the CHMs (D_{CHM}) generated from the eight ~1 ha acquisitions of stereo Phantom 3 DJI RGB imagery (Otero et al., 2018; Fig. 5a, b). Based on the resolution of the TanDEM-X and WorldView-2, H was extracted for 12.5 m × 12.5 m segments that intersected the D_{CHM} and all cells were screened to remove negative or missing values or partial coverages in the overlap area. The average D_{CHM} was then compared separately to the TX_{CHM} and WV_{CHM} to establish the relative correspondence. Historical reference CH data were not however available to support the validation of the $SRTM_{CHM}$.

3.2.5.3. Canopy cover (%). Using the Phantom 3 DJI orthomosaics, an estimate of CC (%) was obtained by first calculating the NDVI from the red and NIR wavebands and then thresholding the resulting image to map the extent of green (productive) vegetation. Whilst not calibrated, comparison of the derived mapping (at < 25 cm resolution) against the RGB orthoimages indicated reliable mapping of green vegetation extent. A 12 m × 12 m grid was then overlain and the percentage of green vegetation within each grid cell (as determined by summing the number of vegetated and non-vegetated pixels) was determined and used to estimate canopy cover (CC; %). Relationships were then established between CC and both the Landsat NDVI and NDMI.

3.2.5.4. AGB (Mg ha^{-1}). AGB estimates obtained from the TDX_{CHM} using both linear and power relationships established with AGB (for African mangrove forests) were compared to those obtained from Hamdan et al. (2013) (adjusted for growth over the subsequent 5–6 years). No field data were available to validate the retrieval of AGB from the $SRTM_{CHM}$. Whilst 114 plot-based measurement of AGB were available, 77 were either a) located close to the edge of the water or clearings where access was difficult or b) had been cleared in subsequent years. For this reason, only those plots (37) contained within the remaining forests and away from the edge were considered, particularly given the likelihood of change occurring in these areas (e.g., erosion, storm damage, further cutting) (Fig. 5c). However, it should be noted that lightning strikes also significantly impact on the structure of mangroves forests, with these leading to discrepencies between field-based and remote sensing observations.

3.2.6. Relationships between retrieved attributes

For the MMFR, large (> 5 ha) segments representing forests of similar age a) from each time-step (i.e., each date of SAR observation) and b) on 29th September 2016, including from the undisturbed protective forests, were identified. Age was estimated in days since 29th July 1988 for each time-step. L_{HH} and/or L_{HV} were extracted from these segments, which were typically located in the centres of areas logged during a harvested period (as determined from the time-series), averaged and converted to σ°. The time since clearance (in days) was also noted, with this associated with the date of each SAR acquisition. Using both sets of data (i.e., from a and b), trajectories were established over the periods where forest were mature, cleared, regenerated and thinned (which typically occurs at 15 and 20 years).

4. Results

4.1. Age class maps

The age class map (Fig. 6), which was based on the time since clearing, indicated that in September 2016, the majority of the productive zone had been cleared over the preceding 29 years. Comparison with local records, visual interpretation of the time-series of Japanese L-band SAR and Landsat sensor data and reference to knowledge from the Forestry Department of Perak Province indicated typical errors of ± 6 months for all age classes. The age class map broadly reflected the distribution of the different logging coupes (including those outlined in the management plan; Ariffin and Mustafa, 2013). However, many contained a diversity of classes albeit within a small range (typically < 2–3 years) because of the staggered nature of timber harvesting within each coupe. This was attributed to the allocation of areas within

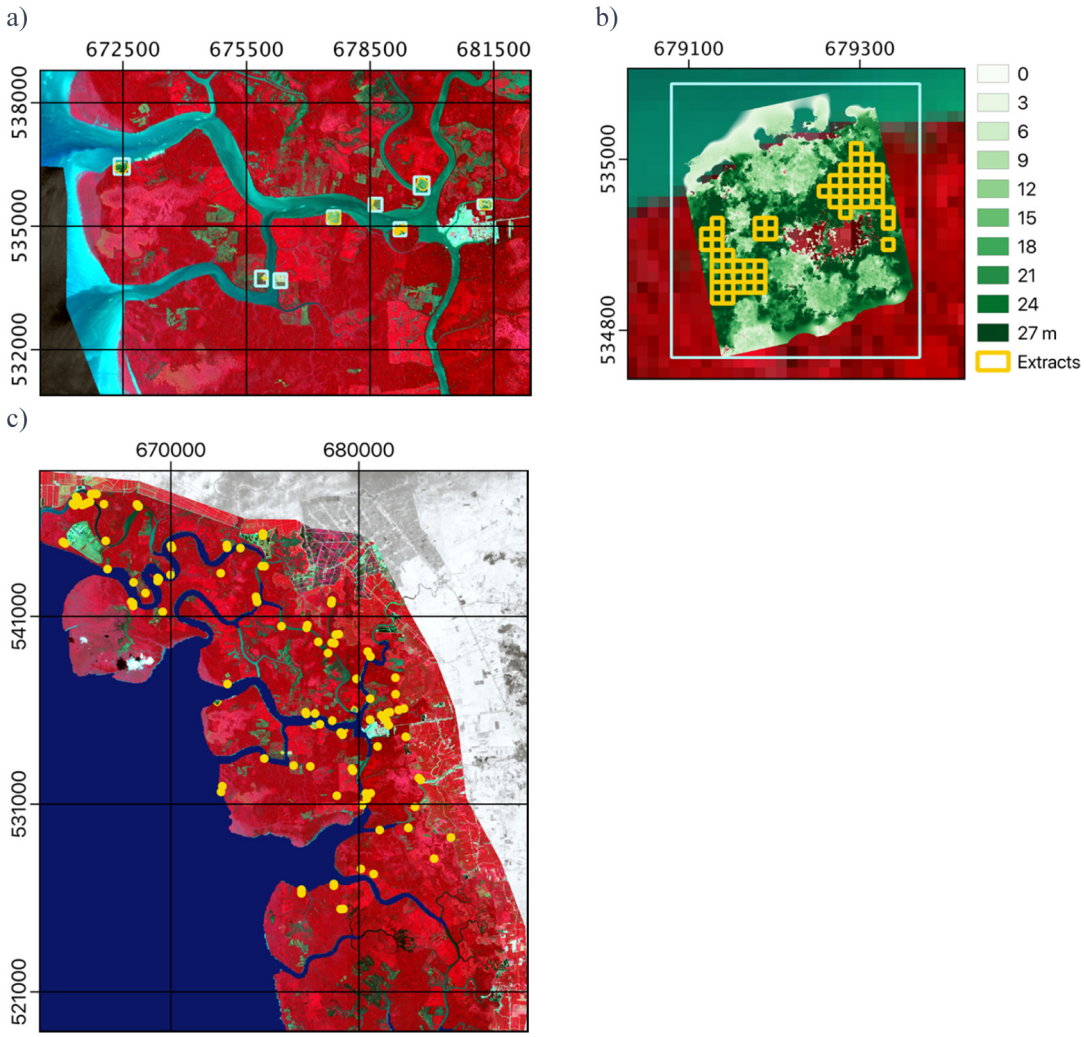

Fig. 5. a) The location of the eight DJI Phantom-3 imagery and 100 m × 100 m (1 ha) extraction zones and b) a close up of the D_{CHM} (height in m) and extraction cells. c) The location of plots surveyed in 2010 by Hamdan et al. (2013) from which stand level estimates of AGB were obtained.

the coupe to different logging companies. Lightning strikes also lead to variability in the age class map and were more prevalent in the older forests and in the protective zones.

4.2. Mangrove height, cover and AGB

A comparison of the D_{CHM} and the ground measures of height within the productive zone indicated a close correspondence (1.3 m; Otero et al., 2018), with this attributed to the relative homogeneity of the forest and the lack of a well-defined understorey. A similarly close correspondence was also observed between mangrove plantation (Navarro et al., 2019) and terrestrial (non-mangrove) forest CH measured on the ground and from a D_{CHM} generated using the SfM algorithm (Panagiotidis et al., 2017). In the more structurally heterogeneous protective forests, the CH estimates were comparable only when the height of the larger trees was considered. The majority of forests considered were however from the productive forest, with one site being in the protective zone but with a relatively closed canopy formed by the larger trees. Hence, the estimates of CH from the DJI Phantom-3 images were considered to be sufficiently robust for comparison with CHMs generated from interferometric SAR and World-view-2 data.

A close agreement between the D_{CHM} and TDX_{CHM} (R^2 = 0.89; RMSE = 1.94; Fig. 7a) was observed, which confirmed the adjustment of the TDX_{CHM} (RMSE = 1.86), although there was an overall bias of 1.06 m (with the D_{CHM} being greater). The agreement between the WV_{CHM} and the D_{CHM} was less (R^2 = 0.75; RMSE = 4.76; Fig. 7b). Following clearing of the forest, a rapid increase in the Landsat-derived NDMI was noted (R^2 = 0.93), with saturation occurring when the CC reached approximately 90% (Fig. 7c). No differentiation in the NDMI of mature forests was observed after 8–10 years of regeneration. A poorer relationship was observed between CC and the NDVI (R^2 = 0.29) and many of the younger (< 8–10 years) supporting NDVI values > 0.5 (Otero et al., 2019). Based on field-measured AGB from the 37 plots positioned within contiguous blocks of forest away from edges, a correspondence with the AGB retrieved from the TDX_{CHM} was observed, with this being greater when AGB was estimated using the power relationship with CH and the equation of Komiyama et al. (2008) (R^2 = 0.53, RMSE = 79 Mg ha^{-1}; Fig. 7d).

4.3. Forest dynamics prior to and since clearance

By combining $L_{HH}\sigma^\circ$ and $L_{HV}\sigma^\circ$ from each time step (i.e., each date of SAR observation) and for forests of the same age, the trends both prior to and following clear events were established (Fig. 8a). At the time of clearing, a rapid increase (by ~5–7 dB) in $L_{HH}\sigma^\circ$ and $L_{HV}\sigma^\circ$ from ~−11–12 dB and −16–17 dB to ~−5 dB and −12.5 dB respectively occurred over a period 2–3 years, with this mirrored by a rapid decrease in the Landsat NDMI as a result of the loss of canopy cover. Both $L_{HH}\sigma^\circ$ and $L_{HV}\sigma^\circ$ then decreased rapidly over the following 7–8 years to

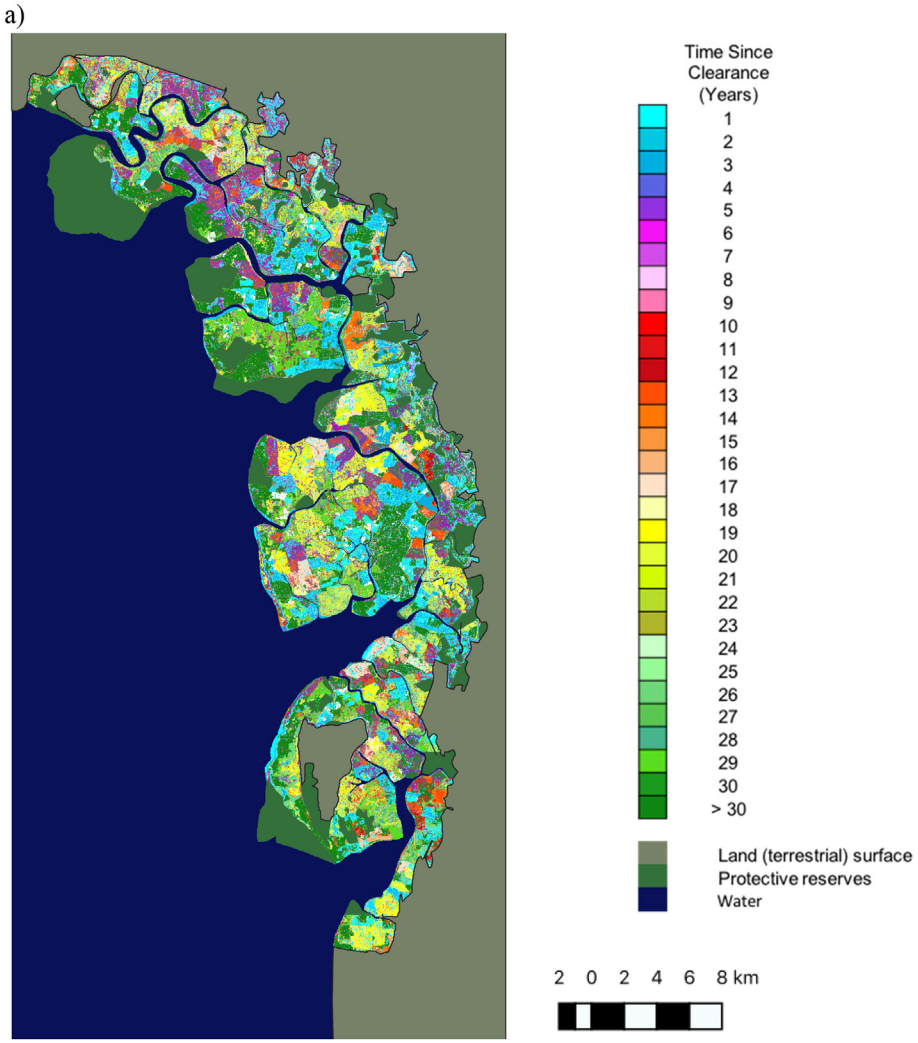

Fig. 6. Map of time since clearance (approximating forest age) on 29th September 2016 for mangroves within the MMFR based on time-series comparison of Landsat-derived NDMI and Japanese $L_{HH}\sigma^{\circ}$ data.

~ -12.5 dB and $-$ 18 dB observed respectively. The NDMI also increased following clearance and attained maximum values (> 90% canopy cover) approximately 8 years after the clearing event. The decrease in L-band σ° continued even though a relatively closed canopy was forming, suggesting that the microwave scattering from coarse woody debris beneath the canopy was still occurring. Thereafter, $L_{HH}\sigma^{\circ}$ and $L_{HV}\sigma^{\circ}$ remained close to these levels although increased slightly until about 17 years since clearing after which $L_{HH}\sigma^{\circ}$ declined slightly whilst $L_{HV}\sigma^{\circ}$ slowly increased to ~ -17.5 dB (similar in magnitude to that of the forest prior to clearance). Differences were observed between the $L_{HH}\sigma^{\circ}$ recorded by the JERS-1 SAR and the ALOS-1/2 PALSAR-1/2, which may, in part, be attributable to variations in the incidence angle range between sensors. The variation in both $L_{HH}\sigma^{\circ}$ and $L_{HV}\sigma^{\circ}$ with forest age, estimated for the 29th September 2016 and extracted from multiple forests coupes, showed a similar pattern (Fig. 8b). Throughout the period, CH increased asymptotically to a maximum of ~22 and 23 m. Four phases therefore became evident from the L-band SAR datasets, with these being associated with a) a rapid increase followed by a decrease in LHHσ° and LHVσ° (over a period of 5–6 years), b) a period of high variability in both LHHσ° and LHVσ°, (6–10 years after clearing) and c) a more coherent period of slight and steady increase in LHHσ° and LHVσ° (10–20 years), with the former reducing slightly thereafter (d).

An increase in the AGB (Mg ha^{-1}) estimated from the TX_{CHM} using the equations of Komiyama et al. (2008) and time-since clearance (years) was obtained (Fig. 9; $R^2 = 0.88$; AGB = 91.369 x ln (Age) -95.839), with this highlighting the potential of using age class information for quantifying AGB across the MMFR. From this relationship, rates of AGB increase were > 20 Mg ha^{-1} yr^{-1} in the first few years of regeneration but decreased steadily to < 5 Mg ha^{-1} yr^{-1} after 13 years. The mean rate of AGB accumulation was 8.36 Mg ha^{-1}. The CH increase in the early years was approximately 1 m yr^{-1} but decreased to about 0.6 m yr^{-1} after 13 years and below 0.4 m after 20 years.

5. Discussion

5.1. Age class estimation

The combined use of both Landsat sensor and Japanese L-band SAR data provided more precise and frequent information on the timing and location of logging activities, and greatly improved spatial estimates of time since clearance and hence the age of forests. The L-band SAR, particularly when acquired at $L_{HH}\sigma^{\circ}$, allowed easy detection of the transition from a mature forest cover to woody debris whilst the Landsat NDMI captured the removal of foliage and hence canopy cover. Whilst the NDVI could also be used, there was less contrast between the recently cleared and pre-cleared forest areas. Limitations of the Japanese L-band SAR included incomplete coverages, but cloud-free data and consistency in between-scene registration and calibration were

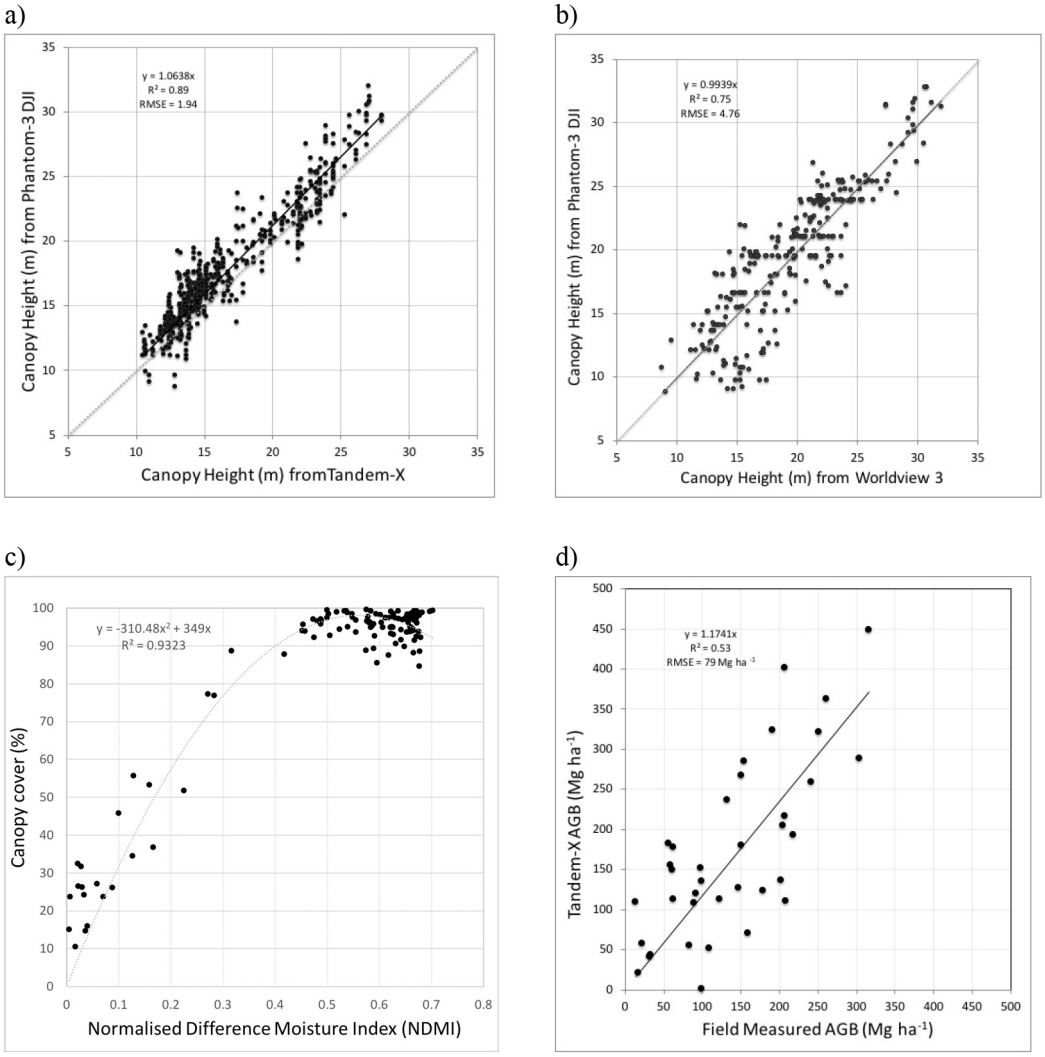

Fig. 7. The correspondence between the D_{CHM} and a) the TX_{CHM} and b) the WV_{CHM} and c) the NDMI and CC(%). d) Comparison of the AGB estimated from the TX_{CHM} and on the ground by Hamdan et al. (2013).

advantageous. The age class map indicated that the majority of mangroves within the productive zone have been cleared since 1988 and are being managed in rotation, as outlined in the Forest Management Plan (Ariffin and Mustafa, 2013).

5.2. Temporal trajectories

Through the rotational cycle and based on the time-series of the Landsat NDMI and Japanese L-band SAR, four change stages (I to IV) could be described and are illustrated in Fig. 10 using UAV RGB images and ground photographs. The UAV images acquired for forests of different age show the progressive covering of woody debris and the formation of a closed canopy and its structural development until maturity. The ground photographs highlight the development of the prop root system within the *Rhizophora*-dominated forests as they approach maturity.

Stage I commences with the cutting of trees and removal of their branches before the logs are taken away from the site. The loss of CC leads to a rapid decrease in the NDMI with a corresponding increase in $L_{HH}\sigma^{\circ}$. Formerly, the canopy would have scattered and attenuated the L-band microwaves as they passed through the volume of plant material. Instead, there is an increase in double bounce interactions with exposed cut stumps and associated overground root systems of the mature *Rhizophora* trees as well as the large branches remaining on the floor. **Stage II** commences with the peak in $L_{HH}\sigma^{\circ}$ and is completed when the minimum is reached after approximately 6–8 years following the clearing event. The **transition to Stage III**, which follows formation of a closed canopy by regenerating or replanted mangroves, can be defined by the period where the increase in the Landsat NDMI cuts across the decrease in $L_{HH}\sigma^{\circ}$. During this period, $L_{HH}\sigma^{\circ}$ continues to decline whereas the NDMI increases, with this attributed to continued scattering from the woody debris located beneath the canopy, which the microwaves penetrate (see also Otero et al., 2019). **Stage III** itself represents the period where, at the start, much of the woody debris has dried and been removed or is in advanced states of decomposition, with this associated with a decreased and minimum $L_{HH}\sigma^{\circ}$. However, through this stage, the decrease is reversed and both $L_{HH}\sigma^{\circ}$ and $L_{HV}\sigma^{\circ}$ are increased by the steady accumulation of AGB within the stems of the regenerating or replanted forest. Thinning of the forests occurs at 15 and 20 years but this was not evident within the time-series of L-band SAR data, despite some temporary loss of AGB. In this stage, a slight decrease in NDMI occurs with this attributed to structural development of the upper canopy. **Stage IV** is only relevant to *Rhizophora*-dominated forests which primarily occur within the productive reserve and its start is defined by the point where σ° at the different polarisations diverge, with $L_{HH}\sigma^{\circ}$ decreasing because of the establishment and maturation of the prop roots and $L_{HV}\sigma^{\circ}$ increasing because of the greater volume scattering from increasing amounts of larger woody material (see

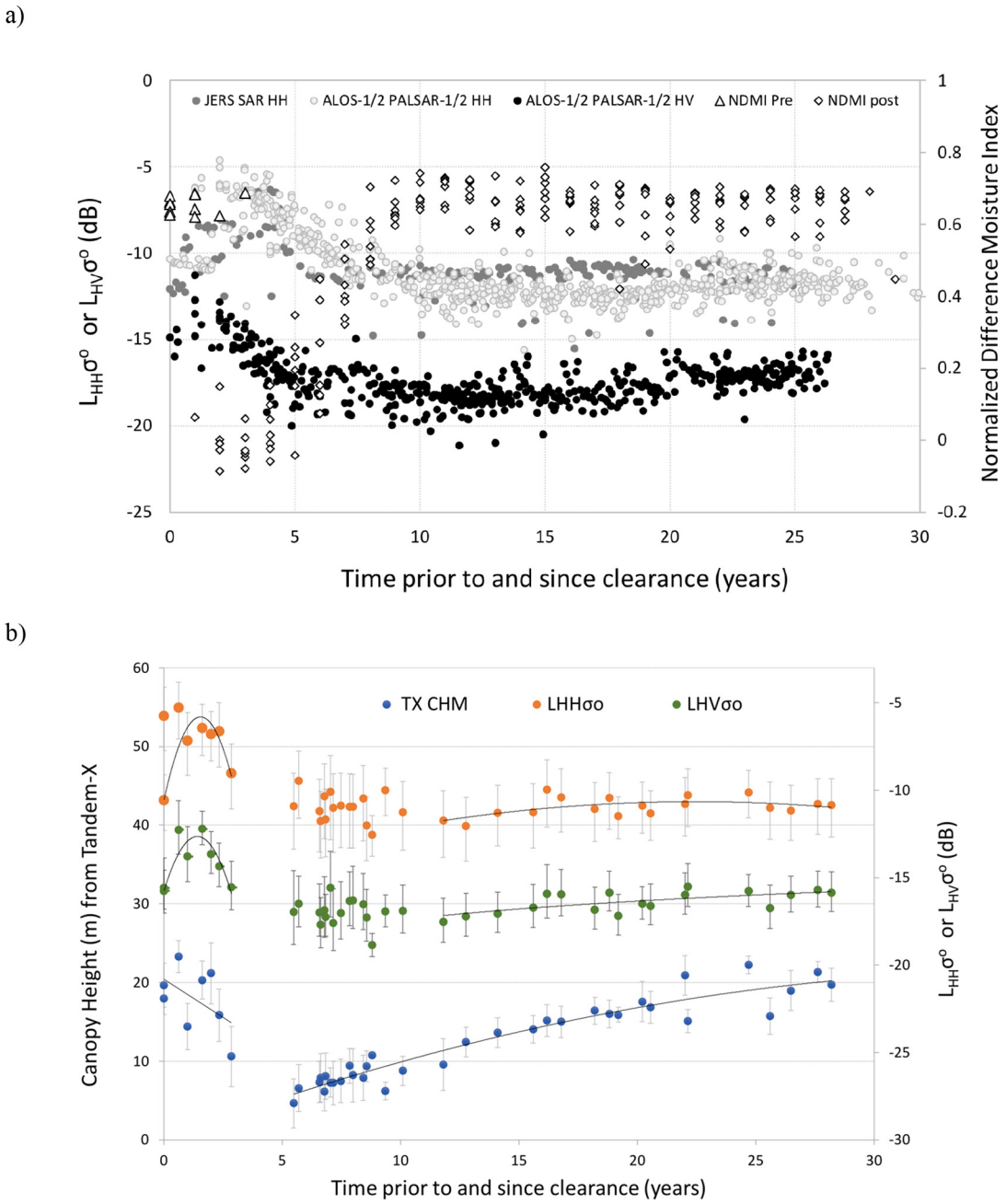

Fig. 8. a). Temporals trend in $L_{HH}\sigma^\circ$ and $L_{HV}\sigma^\circ$ following clearance of the forest based on values extracted a) on the date of L-band SAR acquisition associated with the number of days following (i.e., estimated time since clearing) and b) from ALOS PALSAR HH and HV data acquired on the 29th September 2016 and from multiple forests of varying age, as quantified through time-series comparison of Japanese L-band SAR and Landsat NDMI data (pre and post clearing; the grey box (dashed) represents the period of clear cutting). The incidence angles varied from 36–42°, 36.6–40.9°, 33.7–38.5° and 38.3–42.5° for the JERS-1 SAR, ALOS PALSAR and ALOS-2 PALSAR-2 (beams 6 and 7) respectively.

Fig. 8a). The end of Stage IV is marked by the clearance of the forest at approximately 30 years of age. If left, Stage IV forests would become more structurally complex as natural processes of succession and die-back occur.

5.3. Quantifying structural diversity and biomass

Otero et al. (2018) demonstrated that low cost drones supporting, as a minimum, RGB cameras can be used to retrieve CH estimates at the plot (e.g., 1 ha) level. The close correspondence between the D_{CHM}, TDX_{CHM} and WV_{CHM} confirmed that the method for retrieving CH was viable from Tandem-X interferometric SAR data and satellite stereophotogrammetric data and paves the way for using these data both in the MMFR but also other mangrove forests. Whilst no ground or airborne data were available to validate the $SRTM_{CHM}$, the correspondence with the CH as a function of age (as obtained from the TanDEM-X data) indicated retrievals that were acceptable (Lucas et al., 2020). The TanDEM-X interferometric SAR provided a more consistent estimate of CH compared to that retrieved from stereo WorldView-2 imagery, with this attributed to haze within some areas of the image but also by the textural homogeneity of the vegetation and other surfaces (e.g., including water) within the scene.

The use of CHMs for estimating AGB has been advocated across a range of scales, including by Simard et al. (2018) who utilized SRTM

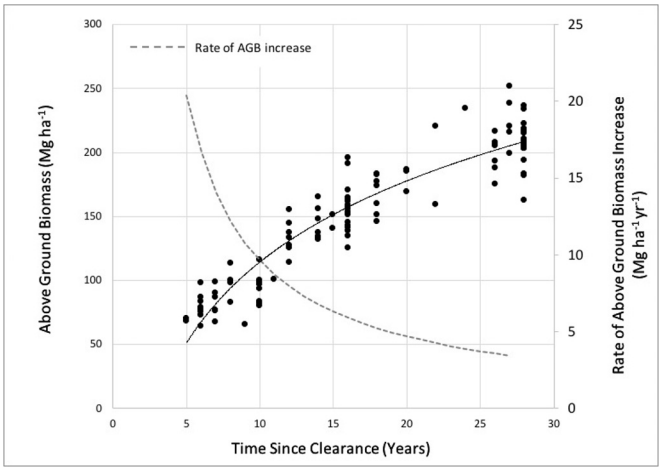

Fig. 9. Relationship between time since clearing and AGB (Mg ha^{-1}) and rates of AGB increase over time.

data to obtain a global retrieval. A recognised limitation of using CH as a surrogate, however, is the large variability in AGB for forests of the same height but with different structural configurations and, to a certain extent, dependency on the dominant species. In the MMFR, for example, the relatively large prop root systems of *Rhizophora* species contribute to the total AGB, with this amount and proportion also varying as a function of age. However, other species (e.g., *Avicennia marina*) do not have prop root systems although may be of the same height. Hence, adjustments for the dominant species is desirable. The retrieval of AGB from CHMs is likely to be robust within the MMFR because of the dominance of *Rhizophora* species throughout the reserve but is likely to be less reliable in areas where several species (including those without prop root systems) co-dominate. For this reason, consideration needs to be given to classifying mangrove species (Sulong et al., 2002; Wang et al., 2004a, 2004b; Dahdouh-Guebas et al., 2005; Neukermans et al., 2008; Satyanarayana et al., 2011; Otero et al., 2016; Rogers et al., 2017). The observed correspondence between forest age and AGB for the MMFR also established that, once the age of the forests is known, a reasonable estimate of AGB can be assigned. However, caution is needed as factors such as disease, climate-related events or site (e.g., as a function of soils, water hydroperiod and tidal inundation) can hinder or promote growth. The changes in CH and AGB over time also provide insights into the growth of forests. CH increase rates were comparable to 30-year rotational mangrove plantations in Papua New Guinea, which averaged 1.3 m yr^{-1} for a 5-year old stand and decreased to 0.7 m yr^{-1} at age 25 (Sillanpää et al., 2017). Rates of AGB change were comparable to that reported by Ong et al. (2004), who reported a mean of 11 Mg ha^{-1} yr^{-1} (measured as the accumulation of biomass and litterfall) and a rate of between 14 and 31 Mg ha^{-1}.

Although there was some sensitivity of $L_{HH}\sigma^{\circ}$ or $L_{HV}\sigma^{\circ}$ to AGB, the complexity of the data over time limited retrieval across the AGB range. Several studies (e.g., Hamdan et al., 2013) have reported that the AGB of mangroves and other forests within the MMFR can be retrieved from L-band data using a general relationship with AGB. However, the complexity of the L-band responses within and between the different change states limits the use of such relationships. For Australian mangroves, Lucas et al. (2007) and Asbridge et al. (2016) reported a decreasing trend in $L_{HH}\sigma^{\circ}$ within taller stands dominated by *R. stylosa*, with this attributed to the development of the prop root system as the trees mature. Whilst a decline in $L_{HH}\sigma^{\circ}$ in the MMFR was observed in the MMFR ~20 years after the event, these were not of the same magnitude (typically 1–2 dB) as those observed in Australia (4–5 dB), which may be attributable to smaller roots systems in the MMFR because of rotational harvesting.

The rapid increase in $L_{HH}\sigma^{\circ}$ and $L_{HV}\sigma^{\circ}$ following clearance of forests has been observed in other situations. For sites in Brazilian Amazônia, Almeida-Filho et al. (2007, 2009) noted respectively that JERS-1 SAR and ALOS PALSAR $L_{HH}\sigma^{\circ}$ were enhanced following deforestation. As with Stone and Woodwell (1988), this was attributed to double bounce scattering from woody debris left on the ground, with the signal also diminishing over time because of drying and removal. The increase in $L_{HH}\sigma^{\circ}$ (2–3 dB) relative to the mature forest was greater in this study (~5–7 dB), with this attributed to the lower response from mature mangroves (Lucas et al., 2007) and a wetter ground (soil) surface or open water associated with cycles of tidal inundation and/or periodic rainfall (Proisy et al., 2002). Soil conditions are uniform and consist primarily of fine mud sediment. Wooden boardwalks are used to remove timber from the coupe for collection at the water's edge, but these represent a small fraction of the total area and were considered to have a minimal impact on the backscattered signal.

SAR simulation models, including those based on wave theory (e.g., Durden et al., 1989) or radiative transfer theory (e.g., Karam et al., 1992, 1995), have been widely used to better understand microwave scattering from within and between vegetation structures and the underlying surface (e.g., by Proisy et al., 2002). However, parameterisation of the models to take account of the varying ground conditions in cleared areas is complex because of the high diversity of dimensions and orientations of woody debris, the different moisture contents of live and dead vegetation, and variations in the extent and depth of surface water. Nevertheless, quantitative ground data could be collected for model parameterisation and augmented by terrestrial or airborne laser scanners or drone imagery. There is also a role for coupling these simulations with inputs from models that quantitatively describe the growth and dynamics of mangroves (e.g., FORMAN; Berger et al., 2008, as undertaken by Kasischke and Christensen (1990) and Ranson et al. (1997)). These models could therefore be adapted to better understand the processes that lead to the enhanced $L_{HH}\sigma^{\circ}$ and, to a lesser extent, $L_{HV}\sigma^{\circ}$, following clearance of forests.

5.4. Implications for management, science and national and international policy

This research provides insight into how to effectively use EO data to inform management of mangroves, including biomass stocks and change. Whilst the length of the time-series (29 years) captured most of the logging cycle, the continued integration of optical (including Landsat-8 Operational Land Imager or OLI and Sentinel-2) and L-band and even C-band (including from Sentinel-1) would allow ongoing monitoring and better advise on the current and future management strategy.

Maintaining an up-to-date record of the AGB of mangroves within the MMFR can be achieved by updating the maps of forest age class. Cross checking of the resulting estimates with available CHMs, as and when acquired, would give some confirmation of the validity of the approach. Indeed, the study has demonstrated that WorldView-2 data are able to provide reliable estimates of CH, which can also be updated as and when cloud free stereo data are acquired. The study has also highlighted the diverse range of information that can be provided by integrating a range of remote sensing data and products. This gives the Malaysian Forest Service the opportunity to continually monitor the impacts of timber extraction to ensure maintenance of a healthy ecosystem and sustainable use of the timber resources and maintain biological diversity (Sleutel, 2016; Barrios Trullols, 2017). The study also provided an indication of rates of both CH and AGB change over the regeneration period, which informs on the dynamics of all forests where the forest age is known. Future work could also investigate the changes in carbon stored in the below-ground components and the transfer to other pools (e.g., the soil and water), with this informed by spatial estimates of AGB. The information obtained can inform current and future investors on the potential impacts of future activities, but also national and international policies aimed at conserving and ensuring

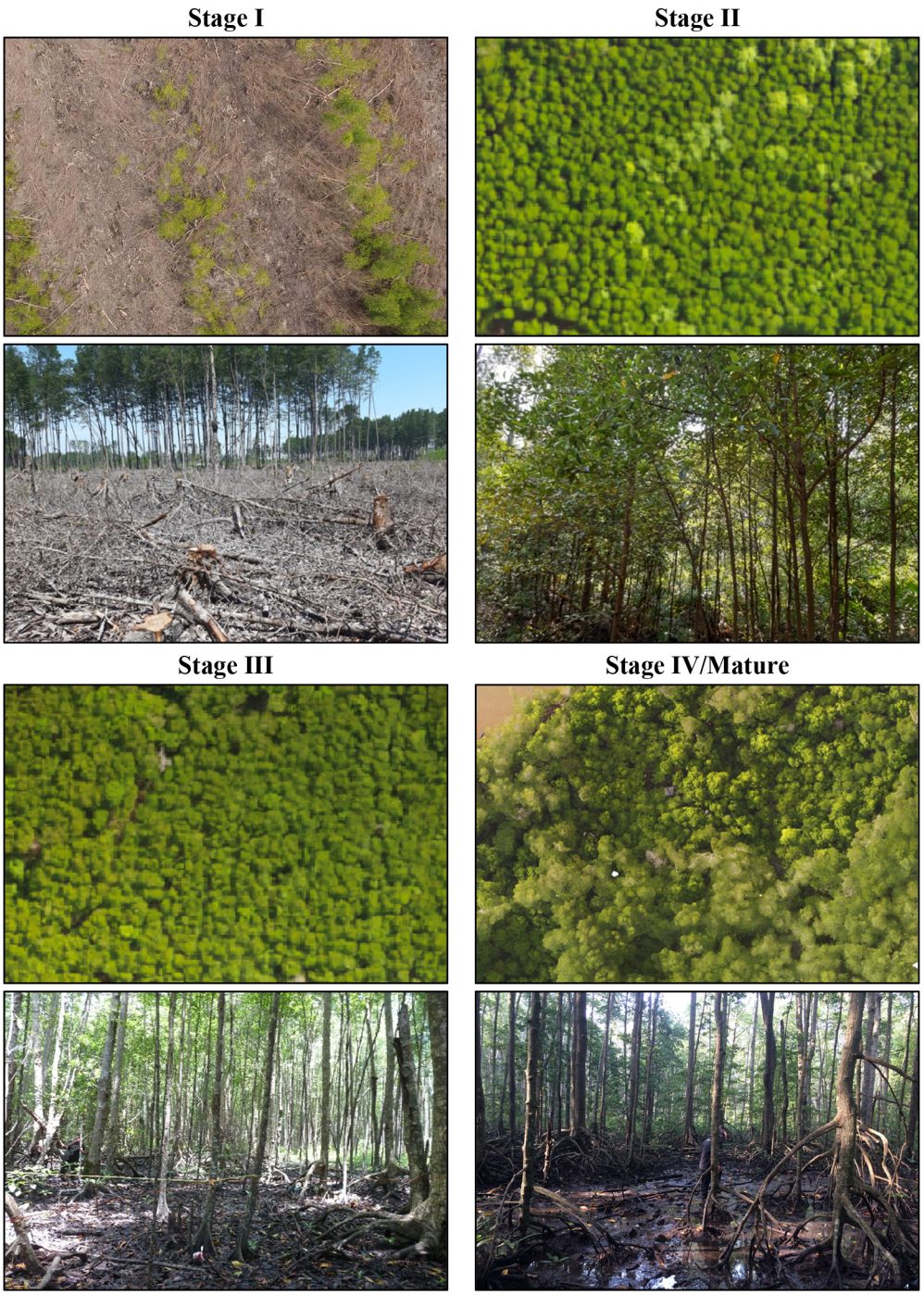

Fig. 10. The four states of change manifested within the time-series of Landsat NDMI and Japanese L-band SAR data and highlighted in the DJI Phantom 3 RGB orthomosaics and ground photographs.

wise use, including in support of the United Nations Sustainable Development Goals (SDGs).

Rotational management of the productive forests within the MMFR has some negative impacts, with Adame et al. (2018) conveying a lower carbon sequestration rate compared to the protective (unmanaged) forests. However, when the carbon (C) sequestration rates of all forests are considered, the MMFR has a positive carbon budget despite losses from the charcoal and pole trade (Barrios Trullols, 2017). Forest management also has other benefits. For example, increases have been observed in all functional guides of avifauna within productive stands of just 7 years and older (Sleutel, 2016). Hence, despite the destructive management associated with clear-cutting every 30 years, the forest can provide functional habitat for some fauna for approximately 22–23 years per rotation and have a positive C budget (provided protective forest area does not decrease). Compared to many other areas in South-East Asia that are cleared for aquaculture or are associated with quick-cash sectors (Duke et al., 2007; Lee et al., 2014; Richards and Friess, 2016), the MMFR does not represent a worst-case scenario. A concern, however, is that if even a small part of the productive zone is affected by, for example, a climate-related event then planned logging sequences might be disrupted with an associated loss of productivity and hence the management and production cycle. The information provided through satellit observations can therefore be used to better plan the rotation cycles and also the allocation of licenses for timber

extraction. In support, Lucas et al. (2020) illustrate how a historical and near real time monitoring system might be implemented using open source software, tools and data.

6. Conclusions

Many studies have focused on using data from single sensors for mapping mangrove extent (e.g., Giri et al., 2011) or retrieving structural attributes such as CC or CH (e.g., Simard et al., 2018). In this study, EO data have been integrated to provide a better understanding of mangrove states and dynamics in response to management carried within the MMFR. The age class map generated using the combination of Japanese L-band SAR and Landsat sensor data highlighted that most mangroves in the productive zones have been harvested over the period 1988 to 2016. The integration of age with CH and CC has led to the identification and description of four stages of change within the rotational cycle.

During the rotation cycle, rapid changes in the amount and horizontal and vertical distribution of woody debris and live plant material occurs as trees are felled, regenerate and are thinned. Such changes have been captured in four stages by the Landsat NDMI (which is sensitive to canopy cover), L-band SAR (relative amounts of dead and live wood), and either interferometric SAR or WorldView-2 stereo optical data (for CHMs). Whilst studies have integrated L-band data in algorithms for retrieving forest AGB, the complexity of microwave interactions with vegetation and the ground surface during the rotational cycle limits their use. For this reason, estimates of AGB are best retrieved from CHMs through new or existing relationships.

The study has also demonstrated the use of low cost drones (in this case, DJI Phantoms) for retrieving estimates of CC and CH over large areas (e.g., 1 ha), with this information providing highly valuable for retrieving or validating these same measures from the Landsat NDMI and interferometric SAR. However, a recommendation is that where such data are collected, these are made publicly available for wider use and ideally collected and processed to an established protocol.

The primary beneficiaries of the research include the Malaysian Forestry Division in terms of assisting with future management of the MMFR, land and mangrove managers in mangrove regions worldwide, and carbon cycle scientists and ecologists. The outcomes are also expected to inform on current and future policy and space agencies of the outcomes of their efforts to launch EO satellites for environmental characterisation, mapping and monitoring.

Declaration of competing interest

The authors declare that they have no known competing financial interests or personal relationships that could have appeared to influence the work reported in this paper.

Acknowledgements

This research was funded by BELSPO (Belgian Science Policy Office) in the frame of the STEREO III Programme – Project Managing Mangrove Forests with Optical and Radar Environmental Satellites (MAMAFOREST) grant number SR/00/323. We thank the Steering Committee members Marc Simard (NASA-JPL), Tiejun Wang (Universiteit Twente) and Daniel Friess (National University of Singapore) for their independent assessments and Joost Vandenabeele and Jean-Christophe Schyns for Belspo STEREO III Programme Management. We also thank the Perak State Forestry Department and the local rangers of the MMFR for their support during the fieldwork and for providing the management plans of the reserve. We thank Muhammad Amir Bin Fisol, Emilia Ashari and Columba Martínez-Espinosa for their collaboration during fieldwork. This study was carried with the approval of the Perak State Forestry Department, Ipoh, Malaysia. Landsat Surface Reflectance products courtesy of the U.S. Geological Survey. The Division of Forestry and Environment, Forest Research Institute Malaysia (FRIM) is thanked for making the field data available for the study. Richard Lucas would like to thank the European Regional Development Fund (ERDF) Sêr Cymru program. David Lagomasino and Lola Fatoyinbo were supported in part by the NASA Carbon Monitoring Systems Program (N4-CMS14-0028 & 16-CMS16-0073). DigitalGlobe data were provided by NASA's NGA Commercial Archive Data (cad4nasa.gsfc.nasa.gov) under the National Geospatial-Intelligence Agency's NextView license agreement.

References

Adame, M.F., Zakaria, R.M., Fry, B., Chong, V.C., Then, Y.H.A., Brown, C.J., Lee, S.Y., 2018. Loss and recovery of carbon and nitrogen after mangrove clearing. Ocean Coast. Manag. 161, 117–126. https://doi.org/10.1016/j.ocecoaman.2018.04.019.

Almeida-Filho, R., Rosenqvist, A., Shimabukuro, Y.E., Silva-Gomez, R., 2007. Detecting deforestation with multi-temporal L-band SAR imagery: a case study in western Brazilian Amazon. Int. J. Remote Sens. 28, 1383–1390. https://doi.org/10.1080/01431160600754591.

Almeida-Filho, R., Shimabukuro, Y.E., Rosenqvist, A., Sánchez, G.A., 2009. Using dual-polarized ALOS PALSAR data for detecting new fronts of deforestation in the Brazilian Amazônia. Int. J. Remote Sens. 30, 3735–3743. https://doi.org/10.1080/01431160902777175.

Ariffin, R., Mustafa, N.M.S.N., 2013. A Working Plan for the Matang Mangrove Forest Reserve, Perak (Sixth Revision). State Forestry Department of Perak (231 pp).

Asbridge, E., Lucas, R., Accad, A., Dowling, R., 2015. Mangrove response to environment change predicted under varying climates: case studies from Australia. Current Forestry Reports. https://doi.org/10.1007/s40725-015-0018-4. (doi:10.1002/ece3.2140).

Asbridge, E., Lucas, R.M., Ticehurst, C. and Bunting, P., 2016. Mangrove response to environmental change in Australia's Gulf of Carpentaria. Ecology and Evolution. https://doi.org/10.1002/ece3.2140. doi:https://doi.org/10.1002/ece3.2140.

Barrios Trullols, A., 2017. Can mangrove silviculture in Matang mangrove forest reserve, Malaysia be carbon-neutral? MSc In: Biology (Specialisation Ecology & Biodiversity), (VUB. 27 pp + 20 suppl).

Berger, U., Rivera-Monroy, V.H., Doyle, T.W., Dahdouh-Guebas, F., Duke, N.C., Fontalvo-Herazo, M.L., Hildenbrandt, H., Koedam, N., Mehlig, U., Piou, C., Twilley, R.R., 2008. Advances and limitations of individual-based models to analyze and predict dynamics of mangrove forests: a review. Aquat. Bot. 89, 260–274. https://doi.org/10.1016/j.aquabot.2007.12.015.

Chave, J., Andalo, C., Brown, S., Cairns, M.A., Chambers, J.Q., Eamus, D., Fölster, H., Fromard, F., Higuchi, N., Kira, T., Lescuire, J.P., Nelson, B.W., Ogawa, H., Puig, H., Riéra, B., Yamakura, T., 2005. Tree allometry and improved estimation of carbon stocks and balance in tropical forests. Ecosyst. Ecol. 145, 87–99. https://doi.org/10.1007/s00442-005-0100-x.

Clough, B.F., Scott, K., 1989. Allometric relationships for estimating above ground biomass in six mangrove species. For. Ecol. Manag. 27, 117–127. https://doi.org/10.1016/0378-1127(89)90034-0.

Dahdouh-Guebas, F., Van Hiel, E., Chan, J.C.W., Jayatissa, L.P., Koedam, N.N., 2005. Qualitative distinction of congeneric and introgressive mangrove species in mixed patchy forest assemblages using high spatial resolution remotely sensed imagery (IKONOS). Syst. Biodivers. 2 (2), 113–119. https://doi.org/10.1017/s1477200004001422.

Duke, N.C., Meynecke, J.-O., Dittmann, S., Ellison, A.M., Anger, K., Berger, U., Cannicci, S., Diele, K., Ewel, K.C., Field, C.D., Koedam, N., Lee, S.Y., Marchand, C., Nordhaus, I., Dahdouh-Guebas, F., 2007. A world without mangroves? Science 317, 41–42. https://doi.org/10.1126/science.317.5834.41b.

Durden, S.L., van Zyl, J.J., Zebker, H.A., 1989. Modelling and observation of the radar polarization signature of forested areas. IEEE Trans. Geosci. Remote Sens. 43 (11), 2612–2626. https://doi.org/10.1109/36.17670.

Fatoyinbo, T., Feliciano, E., Lagomasino, D., Lee, S., Trettin, C., 2017. Estimating mangrove aboveground biomass from airborne LiDAR data: a case study from the Zambezi River delta. Environ. Res. Lett. 13, 025012. https://doi.org/10.1088/1748-9326/aa9f03.

Gillingham, S., Bunting, P., 2014. RFC40: improving performance of raster attribute table implementation for large tables. Available online. http://trac.osgeo.org/gdal/wiki/rfc40_enhanced_rat_support.

Giri, C., Ochieng, E., Tieszen, L.L., Zhu, Z., Singh, A., Loveland, T., Masek, J., Duke, N., 2011. Status and distribution of mangrove forests of the world using earth observation satellite data. Glob. Ecol. Biogeogr. 20, 154–159. https://doi.org/10.1111/j.1466-8238.2010.00584.x.

Hamdan, O., Khariunnisa, M., Ammar, A., Hasmadi, I., Aziz, H., 2013. Mangrove carbon stock assessment by optical satellite imagery. J. Trop. For. Sci. 25, 554–565.

Karam, M.A., Fung, A.K., Lang, R.H., Chauhan, N.S., 1992. A microwave scattering model for layered vegetation. IEEE Trans. Geosci. Remote Sens. 30, 767–784. https://doi.org/10.1109/36.158872.

Karam, M.A., Amar, F., Fung, A.K., Mougin, E., Lopes, A., Le Vine, D.M., Beaudoin, A., 1995. A microwave polarimetric scattering model for forest canopies based on vector radiative transfer theory. Remote Sens. Environ. 53, 16–30. https://doi.org/10.1016/0034-4257(95)00048-6.

Kasischke, E.S., Christensen Jr, N.L., 1990. Connecting forest ecosystem and microwave backscatter models. Int. J. Remote Sens. 11, 1277–1298. https://doi.org/10.1080/

01431169008955093.
Komiyama, A., Ong, J.E., Poungparn, S., 2008. Allometry, biomass, and productivity of mangrove forests: a review. Aquat. Bot. 89, 128–137. https://doi.org/10.1016/j.aquabot.2007.12.006.
Lagomasino, D., Fatoyinbo, T.E., Lee, S., Simard, M., 2015. High resolution canopy height estimation in an African blue carbon ecosystem. Remote Sensing in Ecology and Conservation 1, 51–60. https://doi.org/10.1002/rse2.3.
Lagomasino, D., Fatoyinbo, T.E., Lee, S., Feliciano, E., Trettin, C., Simard, M., 2016. A comparison of mangrove canopy height using multiple independent measurements from land, air, and space. Remote Sens. 8 (4), 327. https://doi.org/10.3390/rs8040327.
Lagomasino, D., Fatoyinbo, T.L., Lee, S.K., Feliciano, E.A., Trettin, C., Shapiro, A.C., Mangora, M.M., 2019. Measuring mangrove carbon loss and gain in deltas. Environ. Res. Lett. https://doi.org/10.1088/1748-9326/aaf0de.
Lee, S.-K., Fatoyinbo, T.E., 2015. TanDEM-X pol-InSAR inversion for mangrove canopy height estimation. IEEE J. Sel. Top. Appl. Earth Observations Remote Sensing 8 (7), 3608–3618. https://doi.org/10.1109/jstars.2015.2431646.
Lee, S.Y., Primavera, J.H., Dahdouh-Guebas, F., McKee, K., Bosire, J.O., Cannicci, S., Diele, K., Fromard, F., Koedam, N., Marchand, C., Mendelssohn, I., Mukherjee, N., Record, S., 2014. Ecological role and services of tropical mangrove ecosystems: a reassessment. Glob. Ecol. Biogeogr. 23, 726–743. https://doi.org/10.1111/geb.12155.
Lucas, R.M., Mitchell, A.L., Rosenqvist, A., Proisy, C., Melius, A., Ticehurst, C., 2007. The potential of L-band SAR for quantifying mangrove characteristics and change, case studies from the tropics and subtropics. Aquat. Conserv. Mar. Freshwat. Ecosyst. 17, 245–264. https://doi.org/10.1002/aqc.833. Special Issue: Radar Applications for Wetlands Management.
Lucas, R.M., Otero, V., Van de Kerchove, R., Satyanarayana, B., Dahdouh-Guebas, F., 2020. Monitoring Matang's Mangroves in Peninsular Malaysia Through Earth Observations: a Globally Relevant Approach. LAND (revised following review).
Lymburner, L., Bunting, P., Lucas, R., Scarth, P., Alam, I., Phillips, C., Ticehurst, C., Held, A., 2019. Mapping the multi-decadal mangrove dynamics of the Australian coastline. Remote Sens. Environ. https://doi.org/10.1016/j.rse.2019.05.004. in press.
Navarro, J.A., Algeet, N., Fernandez-Landa, A., Esteban, J., Rodriquez-Noriega, P., Guillen-Climent, M., 2019. Integration of UAV, Sentinal-1 and Sentinel-2 data for mangrove plantation above ground biomass monitoring in Senegal. Remote Sens. 11, 77. https://doi.org/10.3390/rs11010077.
Neigh, C., Masek, J., Nickeson, J., 2013. High-resolution satellite data open for government research. Eos 94, 121–123. https://doi.org/10.1002/2013eo130002.
Neukermans, G., Dahdouh-Guebas, F., Kairo, J.G., Koedam, N.N., 2008. Mangrove species and stand mapping in Gazi Bay (Kenya) using Quickbird satellite imagery. J. Spat. Sci. 53 (1), 75–86. https://doi.org/10.1080/14498596.2008.9635137.
Njana, M.A., Eid, T., Zahabu, E., Malimbwi, R., 2015. Procedures for quantification of belowground biomass of three mangrove tree species. Wetl. Ecol. Manag. 23, 749–764. https://doi.org/10.1007/s11273-015-9417-3.
Noakes, D.S.P., 1952. A Working Plan for the Matang Mangrove Forest Reserve Perak. Forest Department, Federation of Malaya (178 pp).
Ong, J.E., Gong, W.K., Wong, C.H., 2004. Allometry and portioning of the mangrove Rhizophora apiculata. For. Ecol. Manag. 188, 395–408. https://doi.org/10.1016/j.foreco.2003.08.002.
Otero, V., Quisthoudt, K., Koedam, N., Dahdouh-Guebas, F., 2016. Mangroves at their limits: detection and area estimation of mangroves along the Sahara Desert coast. Remote Sens. 8, 512. https://doi.org/10.3390/rs8060512.
Otero, V., Martinez-Espinosa, C., Dahdouh-Guebas, F., Van De Kerchove, R., Satyanarayana, S., Lucas, R., 2018. Managing mangrove forests from the sky: Forest inventory using field data and Unmanned Aerial Vehicle (UAV) imagery in the Matang Mangrove Forest Reserve, peninsular Malaysia. For. Ecol. Manag. 411, 35–45. https://doi.org/10.1016/j.foreco.2017.12.049.
Otero, V., Van De Kerchove, R., Satyanarayana, B., Mohd-Lokman, H., Lucas, R., Dahdouh-Guebas, F., 2019. An analysis of the early regeneration of mangrove forests using Landsat time-series in the Matang Mangrove Forest Reserve, Peninsular Malaysia. Remote Sens. 2019 (11), 774. https://doi.org/10.3390/rs11070774.
Panagiotidis, D., Abdollahnejad, A., Surovy, P., Chiteculo, V., 2017. Determining tree height and crown diameter from high resolution UAV imagery. Int. J. Remote Sens. 38, 2392–2410. https://doi.org/10.1080/01431161.2016.1264028.
Proisy, C., Mougin, E., Fromard, F., Trichon, V., Karam, M.A., 2002. On the influence of canopy structure on the polarimetric radar response from mangrove forest. Int. J. Remote Sens. 23, 4197–4210. https://doi.org/10.1080/01431160110107725.
Ranson, K.J., Sun, G., Weishampel, J.F., Knox, R.G., 1997. Forest Biomass from Combined Ecosystem and Radar Backscatter Modeling. Remote Sens. Environ. 59, 118–133. https://doi.org/10.1016/S0034-4257(96)00114-9.
Richards, D.R., Friess, D.A., 2016. Rates and drivers of mangrove deforestation in Southeast Asia, 2000-2012. PNAS 113, 344–349. https://doi.org/10.1073/pnas.1510272113.
Rogers, K., Lymburner, L., Salum, R., Brooke, B.P., Woodroffe, C.W., 2017. Mapping of mangrove extent and zonation with the Australian Geoscience Data Cube. Hydrobiologia. https://doi.org/10.1007/s10750-017-3257-5.
Satyanarayana, B., Mohamad, K.A., Idris, I.F., Mohd-Lokman, H., Dahdouh-Guebas, F., 2011. Assessment of mangrove vegetation based on remote sensing and ground-truth measurements at Tumpat, Kelantan Delta, East Coast of Peninsular Malaysia. Int. J. Remote Sens. 32 (6), 1635–1650. https://doi.org/10.1080/01431160903586781.
Schmidt, G.L., Jenkerson, C.B., Masek, J., Vermote, E., Gao, F., 2013. Landsat ecosystem disturbance adaptive processing system (LEDAPS) algorithm description. In: U.S. Geological Survey Open-File Report, 2013–1057, https://doi.org/10.3133/ofr20131057. 17 p.
Shimada, M., Isoguchi, O., Tadono, T., Isono, K., 2009. PLASAR radiometric calibration and geometric calibration. IEEE Trans. Geosci. Remote Sens. 3, 765–768. https://doi.org/10.1109/tgrs.2009.2023909.
Sillanpää, M., Vantellingen, J., Friess, D.A., 2017. Vegetation regeneration in a sustainably harvested mangrove forest in West Papua, Indonesia. For. Ecol. Manag. 390, 137–146. https://doi.org/10.1016/j.foreco.2017.01.022.
Simard, M., Fatoyinbo, L., Smetanka, C., Rivera-Monroy, V.H., Castañeda-Moya, E., Thomas, N., Van de Stocken, T., 2018. Mangrove canopy height globally related to precipitation, temperature and cyclone frequency. Nat. Geosci. 12, 40–45. https://doi.org/10.1038/s41561-018-0279-1.
Sleutel, J., 2016. A Preliminary Assessment of the Impact of the Longtime Silvicultural Management Practiced at the Matang Mangroves on Avifaunal Communities. MSc. Biologie des Organismes et Ecologie - BEVT, ULB (73 pp).
Stone, T.A., Woodwell, G.M., 1988. Shuttle imaging radar. An analysis of land use in Amazonia. Int. J. Remote Sens. 9, 95–105. https://doi.org/10.1080/01431168808954839.
Stringer, C.E., Trettin, C.C., Zarnoch, S.J., Tang, W., 2015. Carbon stocks of mangroves within the Zambezi river delta, Mozambique. For. Ecol. Manag. 354, 139–148. https://doi.org/10.1016/j.foreco.2015.06.027.
Sulong, I., Mohd-Lokman, H., Tarmizi, K., Ismail, A., 2002. Mangrove Mapping Using Landsat Imagery and Aerial Photographs: Kemaman District, Terengganu, Malaysia. Environ. Dev. Sustain. 4 (2), 135–152. https://doi.org/10.1023/a:1020844620215.
Thomas, N., Lucas, R.M., Bunting, P., Hardy, A., Rosenqvist, A., Simard, M., 2017. Distribution and Drivers of Global Mangrove Change, 1996–2000. https://doi.org/10.1371/journal.pone.0179302.
Trettin, C.C., Stringer, C.E., Zarnoch, S.J., 2015. Composition, biomass and structure of mangroves within the Zambezi river delta wetlands. For. Ecol. Manag. 24, 1–14. https://doi.org/10.1007/s11273-015-9465-8.
Wang, L., Sousa, W.P., Gong, P., 2004a. Integration of object-based and pixel-based classification for mapping mangroves with IKONOS imagery. Int. J. Remote Sens. 25 (24), 5655–5668. https://doi.org/10.1080/01431160233129121 5.
Wang, L., Sousa, W.P., Gong, P., Biging, G.S., 2004b. Comparison of IKONOS and QuickBird images for mapping mangrove species on the Caribbean coast of Panama. Remote Sensing of the Environment 91 (3–4), 432–440. https://doi.org/10.1016/j.rse.2004.04.005.
Wessel, B., 2016. TanDEM-X ground segment – DEM products specification document, EOC, DLR, Oberpfaffenhofen, Germany, public document TD-GS-PS-0021, issue 3.2, 2018. [online]. Available. https://tandemx-science.dlr.de/.